Research Square

Preprints are preliminary reports that have not undergone peer review.
They should not be considered conclusive, used to inform clinical practice,
or referenced by the media as validated information.

Lewis acidity-triggered active reconstruction sustains industrial-scale CO2-to-Formate conversion beyond 1500 h

Shaojun Guo

guosj@pku.edu.cn

Peking University https://orcid.org/0000-0002-5941-414X

Na Ye

Peking university https://orcid.org/0000-0003-2895-2751

Kai Wang

Peking university

Zhengyi Qian

Yingjun Tan

Peking University https://orcid.org/0009-0002-6901-9108

Zheng Lin

Peking University

Qizheng Huang

Peking University

Chenglong Sun

Peking university

Hongyu Guo

School of Materials Science and Engineering, Peking University, Beijing, P. R. China., 100871, 5 Yiheyuan Road

Fei Liu

Peking university

Changshuai Shang

Peking University https://orcid.org/0000-0001-7747-6662

Youxing Liu

Beijing University of Chemical Technology https://orcid.org/0000-0003-4407-8785

Yu Gu

School of Materials Science and Engineering, Peking University, Beijing, P. R. China., 100871, 5 Yiheyuan Road

Shipeng Zhang

Peking university

Lu Li
Peking university https://orcid.org/0009-0009-2414-2680
Ying Han
Peking University
Chenhui Zhou
Peking University
Changze Wei
Beijing Institute of Technology
Mingchuan Luo
Peking University https://orcid.org/0000-0001-9772-2154

Article

Keywords:

Posted Date: November 4th, 2026

DOI: https://doi.org/10.21203/rs.3.rs-7049986/v1

License: This work is licensed under a Creative Commons Attribution 4.0 International License.
Read Full License

Additional Declarations: There is **NO** Competing Interest.

Lewis-Acidity-Triggered Active Reconstruction for Cross-Scale Cascade Regulation Enables Industrial CO_2-to-Formate Conversion beyond 1500 h

Na Ye,[1] Kai Wang,[1] Zhengyi Qian,[1] Yingjun Tan,[1] Zheng Lin,[1] Qizheng Huang,[1] Chenglong Sun,[1] Hongyu Guo,[1] Fei Liu,[1] Changshuai Shang,[1] Youxing Liu,[1] Yu Gu,[1] Shipeng Zhang,[1] Lu Li,[1] Ying Han,[1] Chenhui Zhou,[1] Changze Wei,[1] Mingchuan Luo,*[1] Shaojun Guo*[1]

[1]School of Materials Science and Engineering, Peking University, Beijing 100871, P.R. China.

*Correspondence to: guosj@pku.edu.cn and m.luo@pku.edu.cn

Abstract

The electrochemical upgrading of CO_2 remains hindered by its unsatisfied system-level durability to meet industrial requests, which is in part due to the passive reconstruction of catalyst during dynamic operation. Prior research primarily focuses on suppressing such reconstruction with modest improvement in durability. Herein, we report a new Lewis acid-triggered active reconstruction (AR) strategy, enabling super-stable CO_2-to-formate conversion in a membrane electrode assembly (MEA) manner *via* cross-scale cascade regulation. Through this unified AR framework with accelerated reconstruction kinetics, cascade regulations across three scales are synchronously driven: 1) enabling on-demand reconfiguration into dynamically stable atomic-scale rich-low-coordination sites of AR-ITO (active-reconstruction $In_{1.8}Sn_{0.2}O_3/In_9Sn$) through *in-situ* regeneration of defect sites; 2) optimizing the interfacial H_2O/CO_2 microenvironment *via* enhancing $*CO_2^{\cdot-}$ intermediates adsorption and regulating 2H (2-coordinated hydrogen-bonded) interfacial water ratio; and 3) inducing the formation of a catalyst layer with large transport channels that enhances device-scale hydroxide transport and mitigates salt precipitation. This is underpinned by a cross-scale cascade correlation among Lewis acidity, reconstruction kinetics and device-level mass transport-establishing, for the first time, a predictive quantitative principle that bridges atomic, interfacial, and device scales. The optimized AR-ITO catalyst delivers a high $FE_{formate}$ of 91.9% at 1 A cm^{-2} and achieves an unprecedented durability of up to 1500 h at 300 mA cm^{-2} (1.5 A) with the maintained $FE_{formate}$ of 92.0% in MEA electrolyzer. Techno-economic analysis of MEA-based CO_2-to-formate system further demonstrates its application with a gross margin of 34.1%.

Main

The electrochemical CO_2 reduction reaction (CO_2RR) has been recognized as a promising method to transform renewable electricity to high value-added chemicals and fuels (for example formate)[1-4]. Among various electrolyzer designs, the zero-gap membrane electrode assembly (MEA) architecture emerges as a promising candidate for practical applications, owing to its inherent advantages, including a compact system architecture, low ohmic losses and the avoidance of bulky electrolyte [3-5]. However, achieving stable MEA operation exceeding 1000 hours under industrial-level current densities (> 250 mA cm^{-2}) while maintaining high formate selectivity (> 90%) remains a formidable challenge[3,4,6-9]. Consequently, system-level durability under industrial-level current densities has become the primary bottleneck limiting the scalable application of CO_2 electroreduction to formate.

At high current densities, the failure of electrocatalytic system-level durability is fundamentally a multi-scale, cascade-amplified chain reaction. In MEA electrolyzers, this manifests as the coupling and stepwise amplification of multiple interrelated challenges, including catalyst deactivation, imbalances in the interfacial microenvironment, flooding, and salt precipitation, eventually leading to system collapse. Within this chain reaction, we identify catalyst dynamic restructuring as a key trigger. At industrial currents, catalyst tends to undergo unavoidable and uncontrollable passive restructuring. This dynamic process not only directly leads to the formation of the pristine metallic state (accelerating competing hydrogen evolution reaction (HER)) and/or the structural collapse into metastable phases due to thermodynamically driven phase segregation[10-14], but also simultaneously disrupts the interfacial microenvironment, causing local pH imbalance and destabilization of the interfacial water network. Meanwhile, salt precipitation is typically mitigated only through engineering approaches, without being fundamentally resolved, suggesting the involvement of deeper microscopic driving factors. We speculate that, at high currents, catalyst reconstruction may deteriorate mass transport channels from within the catalyst layer, progressively creating conditions that aggravate salt precipitation. Overall, the origin of system-level durability failure may be intrinsically linked to the dynamic restructuring of the catalyst (Fig. **1a**).

Previous research mainly focused on suppressing this passive reconstruction, for instance, through the construction of protective layers.[15,16] (Fig. **1b**). However, despite yielding some improvements, these anti-reconstruction strategies are essentially passive defenses that can only slow the inevitable degradation. They neither completely inhibit catalyst deactivation and microenvironment deterioration nor alter the direction of reconstruction. Consequently, they offer only limited performance gains.

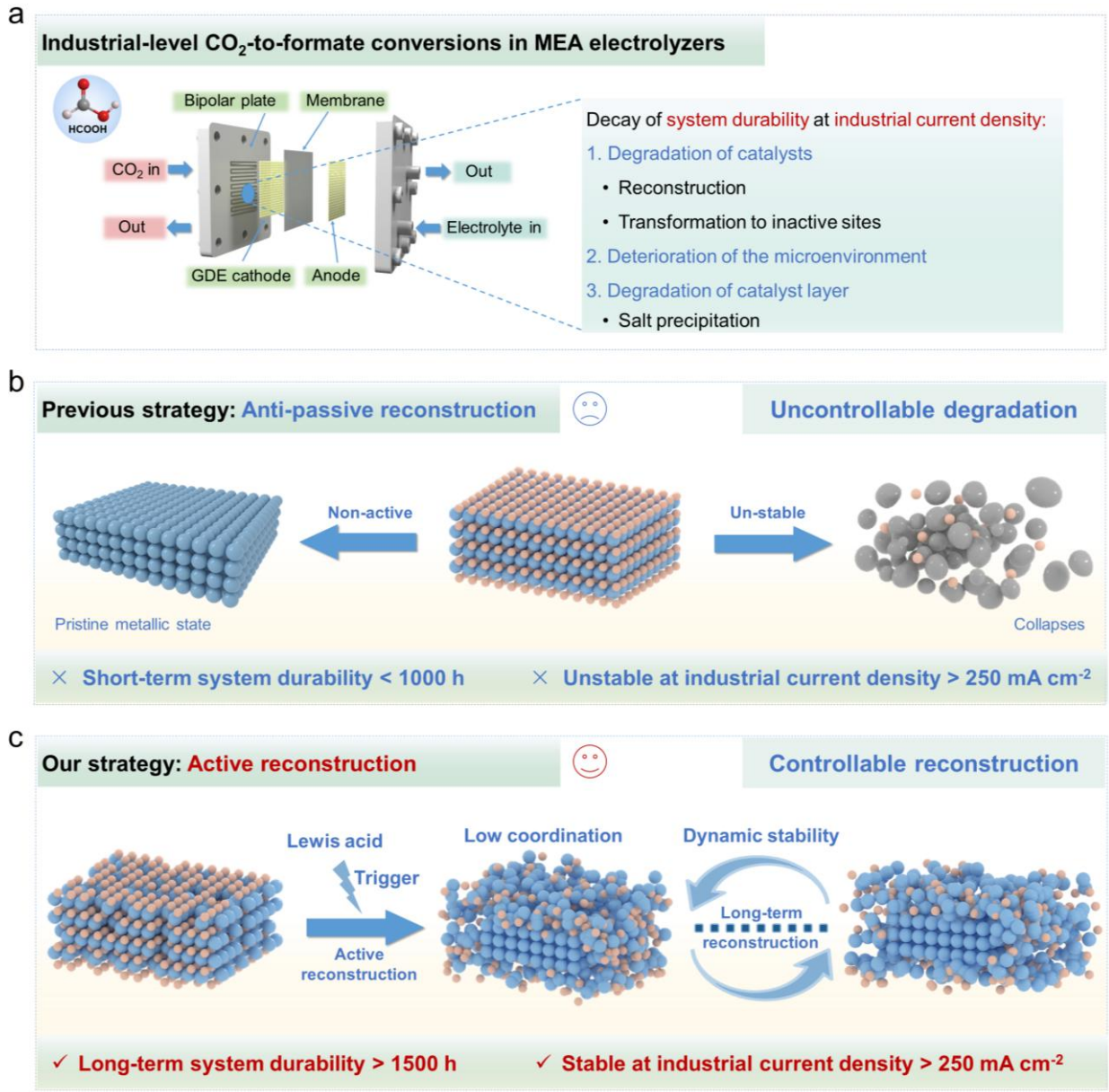


Fig. 1 | Schematic illustration of the performance and structural decay in MEA and our mitigative approach. **a** Schematic illustration for the decay of the durability in MEA electrolyzers. **b** Previous strategies of anti-passive reconstruction. **c** Our strategies of active reconstruction, enabling long-term stability in MEA. This work enables substantial improvements in performance of current density and stability compared with previous state-of-the-art catalysts reported for industrial CO_2RR-to-formate applications ($Bi_{0.1}Sn$[17], s-SnLi[18], Bi[19], Bi_2O_3[20], Zn_1Bi[21], CuS-Bi_2S_3[22], In/N-dG[23]).

Relative to conventional anti-passive reconstruction, we reason that active reconstruction could fundamentally avoid undesired passive reconstruction and sustain long-term industrial-level operations. However, the reconstruction process is generally hard to manipulate, and its effects on the system-level durability are also quite complicated, which has greatly limited its implementations for CO_2RR, especially at industrial scales. Therefore, precisely regulating the reconstruction process, coupling and optimizing the interfacial microenvironment, and establishing a cross-scale correlation between reconstruction kinetics and device-level mass transport represent the key scientific challenges and a promising pathway for achieving long-term CO_2 electroreduction under industrial current densities.

Herein, considering the coordination-unsaturated characteristic of strong Lewis acid (LA) sites, we innovatively proposed a LA-mediated active reconstruction (AR) strategy *via* controllable reconstruction kinetics (Fig. **1c**). The accelerated reconstruction kinetics simultaneously optimize the interfacial microenvironment and device-scale mass transport, thereby bridging the cross-scale link from atomic structure to device-level mass transport Specifically, the AR process constructs a dynamically stable, defect-rich reconstructed layer, wherein the generated unsaturated-coordination sites serve as stabilizing anchors to further optimize and stabilize the CO_2/water interfacial microenvironment. Simultaneously, a catalytic layer with large transport channels spontaneously forms, enhancing device-scale mass transport, and ultimately achieving durable industrial-scale CO_2-to-formate electrolysis. The optimized AR-ITO exhibited a high $FE_{formate}$ of 91.9% at 1 A cm^{-2}. It also maintained superior $FE_{formate}$ (> 92.0%) during the ultra-long 1500-h evaluation at 300 mA cm^{-2} (1.5 A), thus achieving an outstanding formate yield of around 40000 mmol, outperforming all the state-of-the-art performances reported in MEA electrolyzers to date for industrial CO_2-to-formate conversions[17-23]. Overall, our finding highlights great potential of controllable AR, through its cross-domain self-synergy, to markedly enhance system-level durability in CO_2 electroreduction to formate at high currents.

Results and Discussion

Lewis acidity-triggered active reconstruction. To validate the feasibility of Lewis acidity-triggered active reconstruction, we first prepared a series of precatalysts with various Lewis acidity. In detail, the precatalyst of $In_{1.8}Sn_{0.2}O_3$ nanosheets with concave pits was obtained by a template method followed by calcination process (Fig. **2a-2b**, Supplementary Fig. 1-5 and Supplementary Table 1). The X-ray diffraction (XRD, Supplementary Fig. 2) pattern of $In_{1.8}Sn_{0.2}O_3$ nanosheets matches well with that of In_2O_3, demonstrating that Sn was incorporated into In_2O_3, forming solid solutions of $In_{1.8}Sn_{0.2}O_3$. The high-angle annular dark-field STEM (HAADF-STEM) image in Fig. **2a** clearly shows the lattice fringes of 0.29 nm, corresponding to the (222) plane of $In_{1.8}Sn_{0.2}O_3$. The corresponding energy-dispersive X-ray spectroscopy (EDS) elemental mapping (Fig. **2b**) further confirms the uniform distribution of In and Sn in $In_{1.8}Sn_{0.2}O_3$. Both porous In_2O_3 nanosheets formed by the same method and commercial $In_{1.8}Sn_{0.2}O_3$ were selected as control catalysts (Supplementary Fig. 6-7). Fourier transform infrared spectroscopy (FTIR) spectra in Fig. **2c** reveal an enhancement from the intensity of the band at around 1600 cm^{-1} in the order of $In_{1.8}Sn_{0.2}O_3$ nanosheets > In_2O_3 nanosheets > commercial $In_{1.8}Sn_{0.2}O_3$, characteristic of Lewis acidity[14]. The increase in Lewis acidity may be associated with the gradual increase of oxygen vacancies, as suggested by the results of electron paramagnetic resonance (EPR; Supplementary Fig. 4). Herein, based on the magnitude of Lewis acidity, these precatalysts were referred to as $In_{1.8}Sn_{0.2}O_3$ with strong-Lewis acid (s-LA-ITO, 484), In_2O_3 with middle-Lewis acid (m-LA-IO, 311) and commercial $In_{1.8}Sn_{0.2}O_3$ with weak-Lewis acid (w-LA-ITO, 65).

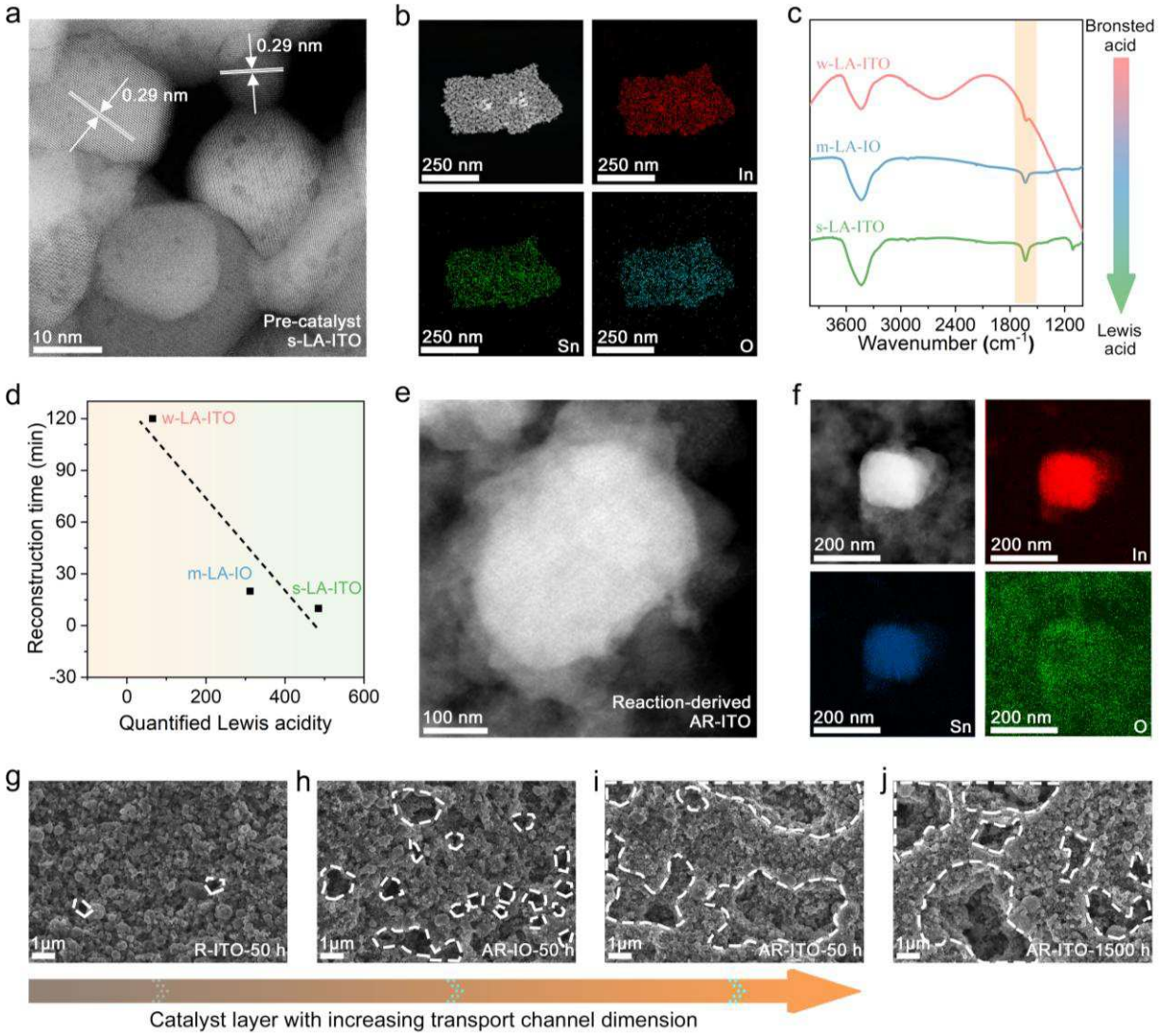


Fig. 2 | Design principle and proof of concept for Lewis acidity-triggered formation of AR-ITO. **a** HAADF-STEM image and **b** EDS elemental mapping images of s-LA-ITO. **c** FTIR spectra of s-LA-ITO, m-LA-IO and w-LA-ITO, with the band of Lewis at around 1600 cm^{-1} highlighted in yellow. **d** A linear-like relationship between quantified Lewis acidity and reconstruction kinetics. **e** HAADF-STEM image and **f** EDS elemental mapping images of AR-ITO after operating in a MEA for 50 h at 300 mA cm^{-2}. **g-i** SEM images of top-layer catalyst layers in R-ITO-GDE (g), AR-IO-GDE (h) and AR-ITO-GDE (i) after 50-h electrolysis, with white dashed lines highlighting transport channels. **j** SEM images of top-layer catalyst layers in AR-ITO-GDE after 1500-h electrolysis, with white dashed lines highlighting transport channels.

To investigate the effect of Lewis acidity of precatalyst on the reconstruction process, we studied the *in-situ* formation of $In_{1.8}Sn_{0.2}O_3/In_9Sn$ catalyst during the CO_2RR over porous $In_{1.8}Sn_{0.2}O_3$ nanosheets. XRD patterns (Supplementary Fig. 8) show that, at industrial-level current densities (300 mA cm^{-2}), the time required for the complete reduction of the s-LA-ITO, m-LA-IO, and w-LA-ITO precatalysts to their metallic states was approximately 10, 20, and 120 minutes, respectively. Quantification of Lewis acidity reveals an approximately linear correlation with this reduction kinetics (Fig. 2d), indicating that Lewis acids can effectively control reconstruction kinetics, thereby governing the reconstruction process.

To investigate the differences in the complete reconstruction of the precatalysts under various Lewis

acids, we operated all catalysts at 300 mA cm^{-2} for 50 h to ensure complete reduction. Combined XRD pattern (Supplementary Fig. 9), high-angle annular dark-field STEM (HAADF-STEM) images (Fig. **2e** and Supplementary Fig. 10a, 11a) and EDS elemental mapping images (Fig. **2f** and Supplementary Fig. 10b, 10c, 11b-11e) show that, after 50 h testing, all catalysts were changed into core-shell structures with an amorphous oxide layers encapsulating the metallic In/InSn core, which was further confirmed by the surface chemical states in X-ray photoelectron spectroscopy (XPS) results (Supplementary Fig. 12) and bulk chemical states in X-ray absorption near-edge structure (XANES) results (Supplementary Fig. 13). The observed phenomenon of *in-situ* surface amorphization is similar to recent studies on water electrolysis and fuel cell[24-26].

From the perspective of macroscopic morphology, SEM images of the electrode surface after 50 hours show that the reconstructed s-LA-ITO catalyst layer developed large transport channels, whereas the reconstructed m-LA-ITO catalyst layer only exhibited a limited number of transport channels with smaller dimensions (Fig. **2g-2i**). The reconstructed w-LA-ITO catalyst layer displayed virtually no visible transport channels (Fig. **2g-2i**). Notably, the evolution trend of transport channel dimensions among the three samples is consistent with the trend in their reconstruction kinetics. This difference primarily originates from the differences in reconstruction kinetics: the rapid reconstruction induced by active reconstruction drives the swift formation of large transport channels, whereas passive reconstruction tends to slowly form a dense structure. The above results indicate that, while the strength of the Lewis acid has no significant effect on the final reconstructed microscopic morphology of the reconstructed catalyst, it can modulate the macroscopic transport channels in the reconstructed catalyst layer by regulating the reconstruction kinetics.

To further support the above conclusion and evaluate the dynamic stability of both the catalyst and the catalyst layer after Lewis acid-induced reconstruction, we examined the composition and morphology of the optimal reconstructed catalyst (s-LA-ITO) after a 1500-h MEA test at 300 mA cm^{-2}. The molar In:Sn ratio remained ~9:1 by the inductively coupled plasma mass spectrometry (ICP-MS), confirming no selective dissolution occurred. At the atomic scale, XRD (Supplementary Fig. 9), fast Fourier transform (FFT, Supplementary Fig. 14) image and line scanning profile (Supplementary Fig. 15) confirmed that the crystal structure and morphology after 1500 h were consistent with those after 50 h of electrolysis, indicating that structural stability of the reconstructed catalyst was achieved under electrolysis conditions. Besides, from a macroscopic structure perspective, SEM images of the top-layer catalyst layers in reconstructed s-LA-ITO-GDE, show that after 1500-hour electrolysis, the reconstructed s-LA-ITO formed a catalyst layer with large transport channels (Fig. **2j**), similar to that after 50-hour electrolysis, indicating that the macroscopic transport channels of the catalyst layer remained dynamically stable after long-term electrolysis. At the same time, the cross-section SEM-EDS mapping images of the reconstructed s-LA-ITO catalyst after the 1500-hour stability test (Supplementary Fig. 16) revealed that In and Sn remained concentrated near the microporous layer (MPL) surface without deep diffusion. These results suggest that no significant macroscopic structural transformation occurred at the electrode level for the reconstructed s-LA-ITO after 1500-hour test. These multiscale analyses, from the atomic scale to the macroscopic electrode level, demonstrate that both the reconstructed catalyst and the catalyst layer induced by Lewis acids exhibited excellent dynamic stability.

To probe the origin of performance differences after LA-induced reconstruction, we conducted EPR, XPS, and EXAFS measurements. EPR results (Fig. **3a**) reveal that, the oxygen vacancy concentration in post-electrolysis catalysts follows the order: reconstructed s-LA-ITO > m-LA-IO > reconstructed w-LA-ITO. This trend aligns with both the reconstruction kinetics and the Lewis acidity of the precatalysts, implying that faster LA-driven kinetics promote the formation of defect-rich structures. Notably, the high oxygen vacancy concentration in the reconstructed

s-LA-ITO remained unchanged at both 50-h and 1500-h electrolysis (Supplementary Fig. 17), indicating robust defect-rich characteristics. For a dynamic reconstruction process, this stability further suggests that Lewis acid-induced defects possess an *in-situ* regenerative capability. This is further supported by the XPS analysis (Supplementary Fig. 18 and Fig. **3b**), which reveals consistent trends in defect concentration across all three catalysts before and after reconstruction. Notably, the s-LA-ITO exhibits the highest oxygen vacancy characteristics before and after reconstruction possess. This suggests that the Lewis acid, acting as an inductive seed, directs the reconstruction kinetics to effectively "inherit" the defect-rich features of the precatalyst, thereby constructing a dynamically stable, defect-rich reconstruction layer.

The Fourier-transformed (FT) EXAFS spectra fitting (Fig. **3c**) and the corresponding Wavelet transform (Fig. **3d**, Supplementary Table 2) display low fitting In-O coordination numbers of 0.4, 0.6 and 1.5 for the reconstructed s-LA-ITO, the reconstructed m-LA-IO and the reconstructed w-LA-ITO, respectively. These coordination numbers show an approximately linear correlation with the quantified Lewis acidity (Fig. **3e**), again supporting that the LA-induced strategy facilitates the formation and dynamic stabilization of low-coordination sites *via in-situ* regenerated defects. We therefore term this distinct process as Lewis Acid-mediated Active Reconstruction (AR) strategy. Accordingly, the post-electrolysis catalysts in this work are referred to as active-reconstruction $In_{1.8}Sn_{0.2}O_3/In_9Sn$ (AR-ITO), active-reconstruction In_2O_3/In (AR-IO) and common-reconstruction $In_{1.8}Sn_{0.2}O_3/In_9Sn$ for commercial precursor (R-ITO).

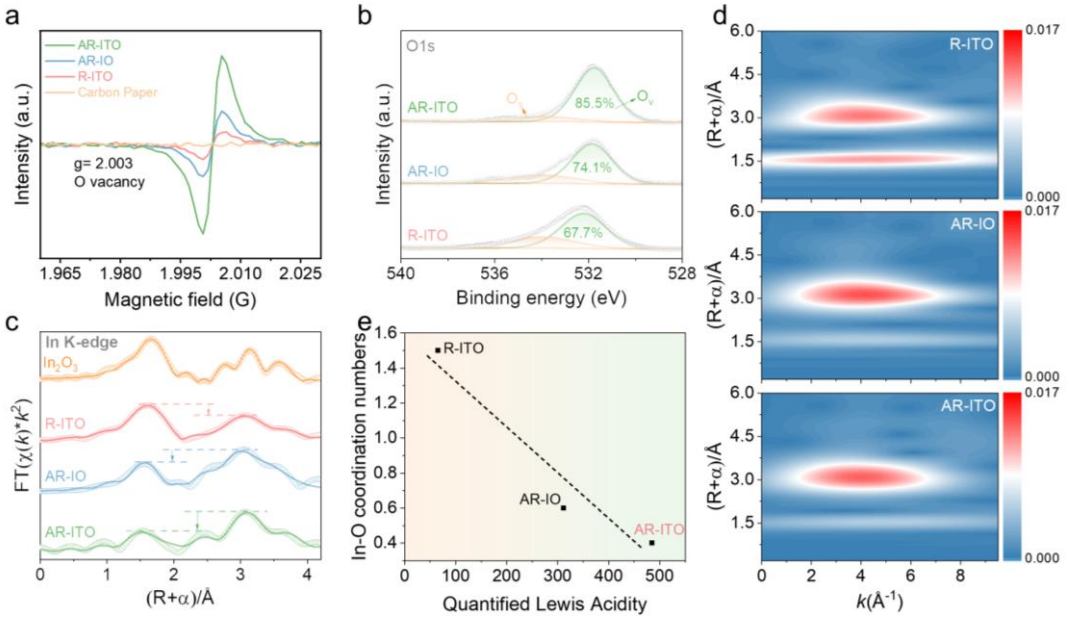


Fig. 3 | **Low-coordinated property of AR-type catalysts with varying oxygen defect**. **a** EPR images of AR-ITO, AR-IO and R-ITO after operating in a MEA for 50 h at 300 mA cm^{-2} and carbon paper. **b** O 1*s* XPS spectra of AR-ITO, AR-IO and R-ITO. **c** Fourier transform of In *k*-edge EXAFS spectra (solid line) and corresponding fitting curves (circles) at R space of AR-ITO, AR-IO, R-ITO and In_2O_3 and the data were *k*3-weighted and not phase-corrected. **d** Wavelet transform for the *k*3-weighted In *k*-edge EXAFS spectra for the R-ITO, AR-IO and AR-ITO catalysts. **e** A linear-like relationship between quantified Lewis acidity and low-coordination sites after reconstruction.

Industrial-level electrochemical CO_2RR performance in flow cells and MEA. To assess the ampere-level performance of these catalysts, they were tested in a flow cell electrolyser in 0.5 M $KHCO_3$. Linear-sweep voltammetry (Fig. **4a-4b** and Supplementary Fig. 19) shows that AR-ITO achieves the highest formate partial current density. It also maintains a Faradaic efficiency (FE) for

formate up to 95.9% (Fig. **4a**) across 200-1000 mA cm^{-2}, far higher than that of AR-IO and R-ITO (Fig. **4b** and Supplementary Fig. 19). In light of the above structural characterizations, the exceptional ampere-level performance of AR-ITO can be attributed to the superior *in situ*-derived intrinsic active site with rich defects in the AR strategy. The pronounced difference between its LSV profiles in CO_2 and Ar atmospheres (Fig. **4a**) for AR-ITO, along with its large electrochemically active surface area (Supplementary Fig. 20, Equation S1), further confirms its inherent activity for CO_2RR. Notably, both AR-ITO and AR-IO exhibit larger metal reduction peaks between 200 and 400 mA cm^{-2} than R-ITO, indicating faster reconstruction kinetics for the LA-mediated catalysts. Above all, these results demonstrate superior CO_2RR performance of AR-ITO at ampere-level current densities and enormous commercial prospects.

To further verify the feasibility of AR-ITO for practical applications, we carried out CO_2 electrolysis in a zero-gap 5-cm^2 MEA electrolyzer (Supplementary Fig. 21-25). Ultimately, AR-ITO achieved a steady durability at 300 mA cm^{-2} over 1500 h in a MEA electrolyzer (Fig. **4c**). Besides, AR-ITO also maintained superior $FE_{formate}$ (> 92.0%) and steady-state cell voltage (~3V) at a ultra-steady level, thus achieving a formate yield of 40000 mmol and full-cell energy efficiency of 43.1% (Equation S2). This surpassed all the state-of-the-art performances reported in MEA electrolyzers to date for industrial-level CO_2-to-formate electrolysis (Fig. **4c**, generally, the notable deterioration of most of catalysts reported is significant after hundreds of hours.)[17,18,21-23]. Notably, AR-ITO almost retained the beginning $FE_{formate}$ and cell voltage after the 1500-h evaluation (Fig. **4d**). The stability obtained was limited by the corroded anode plate by the electrolyte (Supplementary Fig. 26), while the true lifetime of the catalyst may be much longer. Additionally, combined HRTEM, XRD, EPR and XAS results confirm that the robust AR-ITO catalyst maintained its original reconstruction structures after the 1500-h evaluation, further indicating that the intrinsic structural stability of post-electrolysis catalyst was achieved.

The techno-economic analysis (TEA) reveals that the MEA-based CO_2-to-formate system delivers a net profit of $140,448 *per* ton. This value is nearly equivalent to one-third of the market price ($420,000 *per* ton), highlighting the economic viability and large-scale application potential of our process (Supplementary Fig. 27).

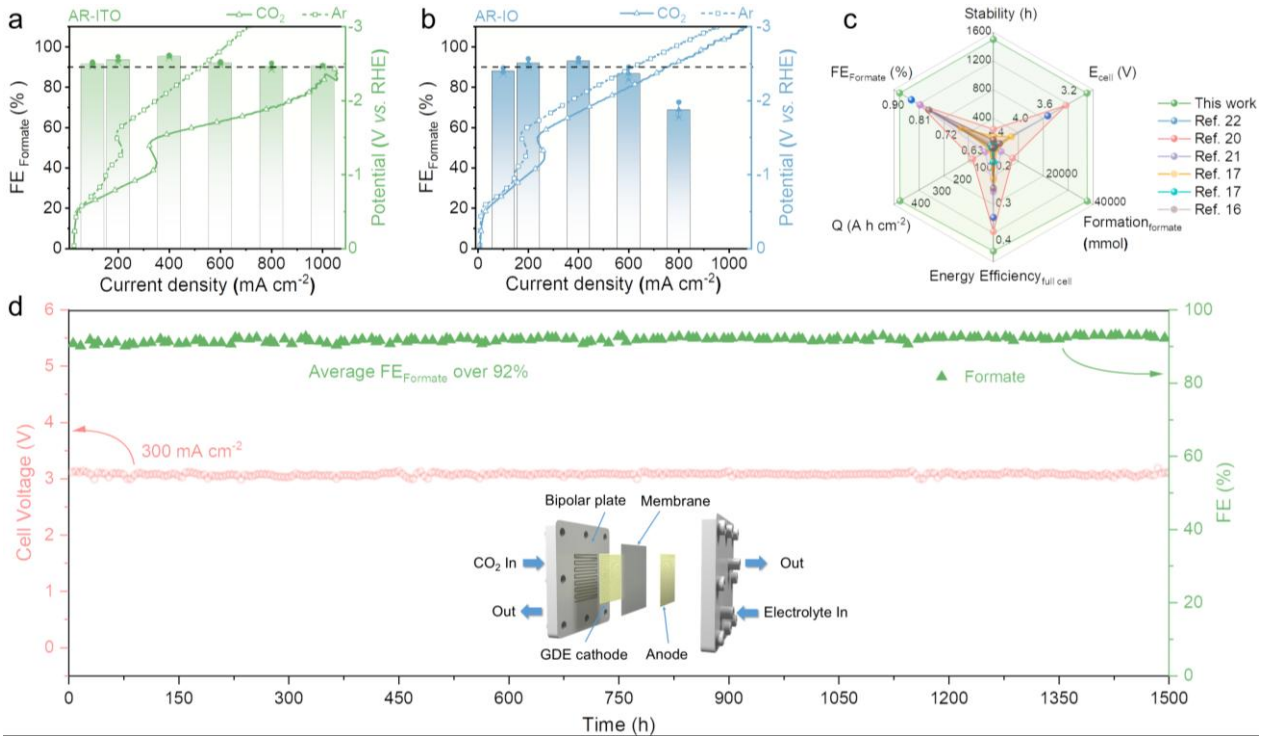


Fig. 4 | CO_2RR performances of AR-ITO in flow cells and MEA at industrial scales. **a-b** Polarization curves over AR-ITO (**a**) and AR-IO (**b**) under Ar (dashed line) and CO_2 (solid line) atmospheres in 0.5 M $KHCO_3$, and FE of formate on AR-ITO (**a**) and AR-IO (**b**) with various current densities in 0.5 M $KHCO_3$ in flow cells. The error bars mean the s.d. (n = 3 replicates); data are shown as mean values ± s.d. **c** Comparison of CO_2RR performance over AR-ITO and the reported state-of-the-art catalysts for industrial CO_2RR applications in MEA electrolyzers (durability, $FE_{formate}$, Q, full-cell energy efficiency, yield of formate and E_{cell}). **d** Durability test (pink line) and $FE_{formate}$ (green line) over AR-ITO at 300 mA cm^{-2} for 1500 h in 5-cm^2 MEA electrolyzers. Inset presents a schematic representation for the MEA electrolyzer.

Reaction microenvironment modulation. To gain molecular-level insights into this interfacial microenvironment and identify key reaction intermediates, we conducted *in situ* attenuated total reflection-surface enhanced infrared absorption spectroscopy (ATR-SEIRAS) studies and *operando* Raman spectroscopy under MEA conditions (Fig. **5**, Supplementary Fig. 28-32 and Supplementary Table 3). In this work, ATR-SEIRAS spectra were collected from 0 to 0.9 V, a potential range that covers the operating current density of 0-300 mA cm^{-2} in both the flow cell (Fig. **4**) and the MEA (where the measured cathode voltage difference of the MEA is shown in Supplementary Fig. 30-31). *Operando* Raman spectra were collected in a MEA over a current density range of 20 - 300 mA cm^{-2} (Supplementary Fig. 32).

In Fig. **5a**-**5b** and Supplementary Fig. 33, a band around 1377 cm^{-1} and 1540 cm^{-1} are observed, which can be attributed to the symmetric stretching vibration and asymmetric stretching vibration of *OCHO intermediate, respectively[27,28]. Additionally, we find that as the potential shifts negatively, the coverage of the band at around 1377 cm^{-1} continuously increases (Fig. **5a**-**5b**). By correlating the quantified peak areas of the band at around 1377 cm^{-1} at various potentials with the current density, a significant linear relationship is observed (Fig. **5c** and Supplementary Fig. 34), indicating that the accumulation of the *OCHO intermediate directly determines the rate of formate production in the CO_2RR process. Furthermore, a band at around 1250 cm^{-1} associated with $*CO_2^{\cdot-}$ that arises from the adsorption and activation of CO_2 can also be observed[29-31]. Simultaneously, two characteristic peaks located at 1250 $cm^{-1}$and 1690 cm^{-1} are observed to display a synergistic enhancement with the negative shift of the potential. The positive correlation in the intensity of these two peaks further confirms the assignment of the $*CO_2^{\cdot-}$, consistent with the reported literature[31,32]. In addition, a weak shoulder peak at ~1220 cm^{-1} appears next to the main band at ~1250 cm^{-1} (Fig. **5a**), accompanied by bands at ~1740 cm^{-1} and ~1130 cm^{-1}. These three features can be attributed to the C-O stretching vibrations, C=O stretching vibrations, and out-of-plane C-H deformations in formate, respectively[27]. This provides direct molecular-level evidence that defect-rich AR-ITO follow the formate pathway.

In addition, *operando* Raman spectra under MEA conditions reveal that the band at around 3600 cm^{-1} (Fig. **5d**-**5e**) can be related to the stretching vibration of OH[33-35]. Notably, there is also a close connection between the stretching vibration of OH and the behavior of the interfacial water, as it showcases significant effects on the interfacial water microenvironment and the associated hydrogen transfer, which are key processes involving in CO_2RR[34,36-38]. To quantitatively evaluate the effect of the interfacial water microenvironment on CO_2RR, the broad signal at around 3600 cm^{-1} can be assigned into three bands at 3600 cm^{-1} (free water), 3450 cm^{-1} (2-coordinated Hydrogen-bonded water, 2H water) and 3270 cm^{-1} (4-coordinated hydrogen-bonded water, 4H water, Fig. **5d**-**5e**, Supplementary Fig. 35)[36,37]. The difference in the detailed ratios of three bands in Fig. **5f** indicates a transition from 2H water to 4H water in the sequence of AR-ITO, AR-IO and R-ITO, implying a change in the predominant structures of the interfacial water. Specifically, the fraction of 2H water on AR-ITO (50.0%) is higher than those on AR-IO (42.2%) and R-ITO (35.8%), which means that AR-type reconstructed catalysts are prone to forming a substantial fraction of weakly H-bond water

associated with the weakened H-bond network[37,38] relative to common reconstruction.

Ab-initio molecular dynamics (AIMD) results (Fig. **5g-i**, and Supplementary Fig. 36) further corroborate this. Specifically, relative to non-AR catalysts, the AR-type reconstructed catalysts exhibit more interactions with H-down-orientated interfacial water (Fig. **5g**, **5h** and Supplementary Fig. 37). The resulting radial distribution function for In-O results (Fig. **5i**) shows that the interactions between In and O in water molecules are less pronounced in the AR-type catalysts, suggesting that AR-type reconstructed catalysts preferentially adopt the O-up configuration, which favors the formation of a weakened H-bond network[33,39]. These results also demonstrate that the dynamic transformation of the interfacial water is sensitive to the reconstruction kinetics. Impressively, there is a negative linear relationship between the fraction of 2H water and the FE_{H2} at large currents (Fig. **4a-4b** and Supplementary Fig. 19), suggesting that the enrichment of 2H water can inhibit competitive HER. These finding strongly suggests that AR-type reconstructed catalysts affect the $*CO_2^{\cdot-}$ intermediates formation and the reconfiguration of H-bonds networks within interfacial H_2O microenvironment, i.e., mediating interfacial H_2O/CO_2 microenvironment.

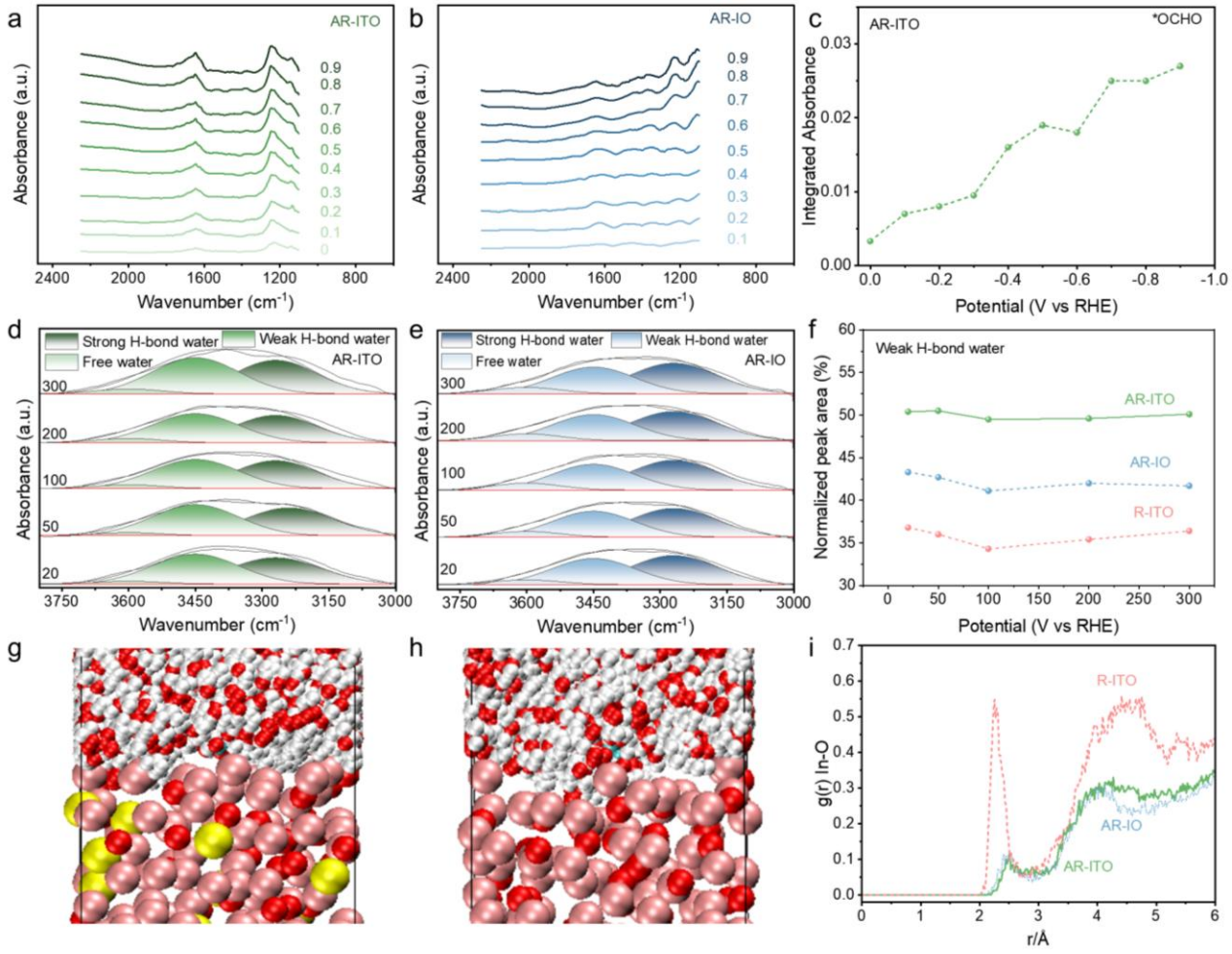


Fig. 5 | *In situ* spectroscopic proof for microenvironment modulation. **a-b** Potential-dependent *in situ* ATR-SEIRAS spectra over the AR-ITO (**a**) and AR-IO catalysts (**b**). **c** The coverage of *OCHO over the AR-ITO catalysts at various potentials. **d-e** *Operando* Raman spectra and corresponding fitted bands of interfacial water at various current densities from 3800 to 3000 cm^{-1} over the AR-ITO (**d**) and AR-IO (**e**) catalysts. **f** *Operando* Raman spectroscopy-derived fitted percentage of various types of interfacial water at various current densities over the AR-ITO, AR-IO and R-ITO catalysts. **g-h** Representative snapshots of the AIMD-simulated interfaces structures over the AR-ITO (**g**) and

AR-IO (**h**) catalysts. **i** Radial distribution function for In-O over the AR-ITO, AR-IO and R-ITO catalysts.

Mechanistic mechanism. To investigate the mechanism by which Lewis acid-induced AR-type reconstruction promotes CO_2-to-formate electrolysis, we conducted density functional theory (DFT, Supplementary Fig. 38). As illustrated in Fig. **6a**, the free energy of *OCHO on AR-ITO is lower than those on AR-IO and R-ITO, indicating that AR-type reconstruction promotes the generation of *OCHO species, which are critical intermediates for the process of CO_2RR to formate. This is consistent with the correlation conclusions derived from the quantified *OCHO species in *in situ* ATR-SEIRAS and the electrocatalytic performance results, which experimentally validates the crucial role of *OCHO species in the reaction pathway as predicted by DFT results.

To investigate the origin of the formate performance enhancement of AR-ITO, we correlate low-coordinated sites, p-band center, and $FE_{formtae}$ at high current densities, and find that all three are linearly related (Fig. **6b**, Supplementary Fig. 39-41). These results indicate that relative to common passive reconstruction, the AR-type reconstruction is more favorable for the abundance of low-coordinated sites and down-shifted p-band center. Meantime, based on active reconstruction, the Sn doping would further facilitate the low-coordinated sites. Furthermore, the linear correlation between the coordinated sites and $FE_{formtae}$ (Supplementary Fig. 39) indicates that the abundant low-coordinated sites in AR-ITO catalysts can act as active sites to boost the industrial-level CO_2-to-formate electrolysis. This is consistent with the large ECSA and high adsorption energy of *OCHO (-0.64 eV, -0.60 eV and -0.46 eV for AR-ITO, AR-IO and R-ITO, respectively) brought by low-coordinated sites properties.

To further elucidate the origin of enhanced system stability of AR-ITO towards CO_2RR under high performance, we investigated across multiple scales, ranging from the atomic level to the interface and device levels. 1) From the catalyst perspective, as confirmed earlier, the combination of HRTEM, XRD, EPR and XAS results reveals that, the AR-ITO catalyst retains its morphology and low-coordinated structure after 1500-h electrolysis, demonstrating that the AR-type reconstruction achieves dynamic stability through *in-situ* regeneration of abundant defect sites. This is also further confirmed by the corresponding maintained In-O bond in *in situ* Raman (Supplementary Fig. 42), enhanced Density Derived Electrostatic and Chemical (DDEC) bond order (Supplementary Fig. 43, Supplementary Table 4) and vacancy formation energy (Supplementary Fig. 44) results on AR-type reconstructed catalysts. 2) From the reaction microenvironment perspective, as evidenced by *in situ* ATR-FTIR, *operando* Raman spectroscopy and DFT results, the abundant 2H interfacial water (~50.0%) associated with the inhibited competitive HER and the enhancement of $*CO_2^{\cdot-}$ intermediates on AR-type reconstructed catalysts imply that AR reconstruction optimizes the interfacial H_2O/CO_2 microenvironment. 3) From the electrode perspective, SEM results of the catalysts layer after testing reveal that the evolution trend of transport channel dimensions is consistent with the reconstruction kinetics (Fig. **6c**). The AR-ITO catalyst layer maintains a dynamically stable structure with transport channels after 1500 h electrolysis. To further probe the role of this transport channels, finite element simulations were performed (Fig. **6d-6g**). The results show that within the AR-ITO catalyst layer (**6d-6e**), OH^- transport resistance is low, enabling rapid diffusion from the inlet to the outlet. In contrast, on R-ITO (**6f-6g**), OH^- transport is hindered; over time, substantial OH^- accumulates near the inlet, with limited diffusion to the outlet. These finite element simulation results demonstrate that the catalyst layer with large transport channels driven by active reconstruction significantly promotes hydroxide diffusion, effectively alleviates local alkaline concentration buildup, and suppresses the potential for salt precipitation at the microscopic driving force level. This also establishes, for the first time, a cross-scale correlation between reconstruction kinetics and device-scale mass transport.

Furthermore, under identical operating conditions, the R-ITO catalyst exhibited salt precipitation and rapid performance decay (Supplementary Fig. 45), whereas the AR-ITO sustained long-term stable operation for 1500 h. This confirms that, the catalytic layer with large transport channels fabricated *via* AR can effectively inhibit salt precipitation and support long-term system-level stability.

Overall, our multi-scale characterizations and simulations collectively demonstrate that the AR strategy proposed herein, for the first time, integrates atomic-scale site regeneration, interfacial reaction microenvironment optimization, and device-scale mass transport enhancement (Fig. **6h**). This provides an advanced methodology to address the long-term system-level stability challenge in industrial CO_2RR applications.

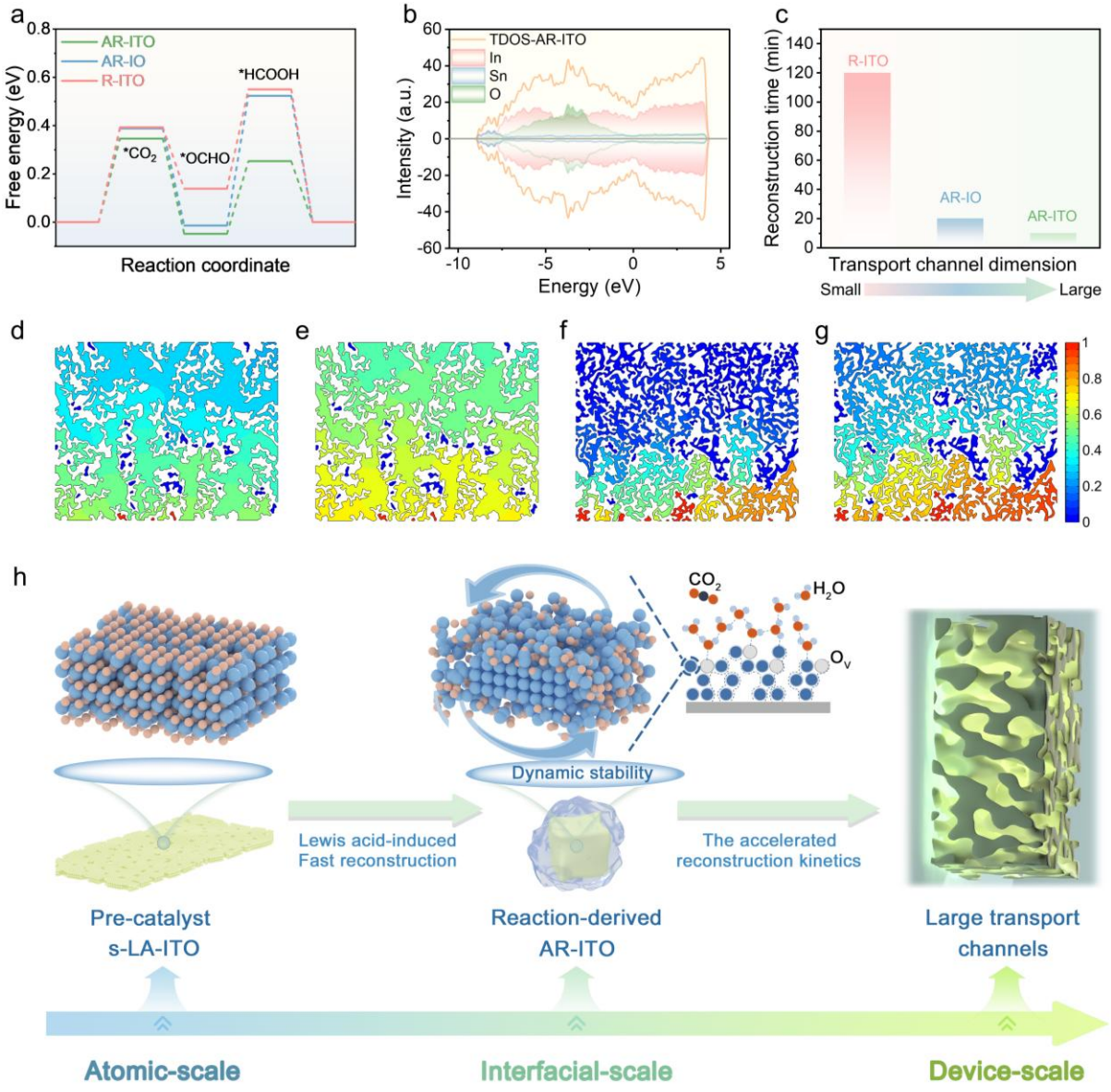


Fig. 6 | Mechanism analysis of the AR strategy on the AR-ITO catalyst. a Free energy diagrams of CO_2RR to formate on AR-ITO, AR-IO and R-ITO. **b** DOS of AR-ITO. **c** Transport channel dimension of the catalyst layer as a function of the reconstruction kinetics. **d-g** Finite element simulation results for the OH^- distribution in catalyst layers of the AR-ITO (d, e) and R-ITO catalysts (f, g) under the same time gradient. **h** Proposed cross-scale cascade regulation mechanism of AR strategy.

Conclusions

We put forward a Lewis acid-mediated active reconstruction (AR) strategy that transforms catalyst reconstruction under high-activity and high-current-density conditions from an uncontrollable passive degradation into a directional process with predictable trajectory and controllable kinetics. Based on this, we establish a cross-scale correlation: Lewis acidity is linearly correlated with reconstruction kinetics, and the accelerated kinetics, in turn, not only regenerates low-coordination sites *in situ* and optimizes the interfacial microenvironment, but also induces the formation of a catalyst layer with large transport channels that enhances mass transport. This correlation bridges, for the first time, the atomic-scale driving force, the interfacial microenvironment, and device-scale mass transport. Combined experimental and theoretical results reveal that, the implement of the AR-type reconstruction can stably and continuously generate unsaturated-coordinated sites due to *in-situ* regenerated abundant defect sites. This depends on Lewis acidity-mediated reconstruction kinetics, thereby achieving dynamically steady intrinsic structure, thereby upgrading the catalyst from static "structural design" to dynamic "evolutionary regulation". Meanwhile, the abundant unsaturated-coordinated sites can also act as a steady anchor to modulate the $*CO_2^{\cdot-}$ intermediates adsorption and the 2H interfacial water ratio to optimize the interfacial H_2O/CO_2 microenvironment. Concurrently, the accelerated reconstruction kinetics spontaneously construct a catalytic layer with large transport channels at the device scale, improving OH^- transport and mitigating salt precipitation. This effectively breaks the cross-scale cascade-amplification chain that leads to system-level failure. The optimal AR-ITO catalyst, shows a remarkable CO_2RR performance, delivering a high $FE_{formate}$ of 91.9% at 1 A cm^{-2} in flow cells and an unprecedented durability of up to 1500 h at 300 mA cm^{-2} with the maintained $FE_{formate}$ of 92.0% in MEA electrolyzers, achieving a record formate yield of 40000 mmol, outperforming all the performances reported in MEA electrolyzers to date. A techno-economic analysis of MEA-based CO_2-to-formate system shows that this approach can achieve a gross margin of 34.1%, demonstrating profitability potential.

Methods

Synthesis of s-LA-ITO. In a typical synthesis of s-LA-ITO, $In(NO_3)_3$ (1 mmol), $SnCl_4$ (0.11 mmol), 25 g of glucose and 5 g of urea were introduced into ultrapure water (50 mL) with concentrated HNO_3 (2 mL) and ultrasonically dispersed for 10 min. The resulting homogeneous solution was then heated at 140 ℃ for 24 h. Finally, the mixture was calcined in air at 500 ℃ for 12 h to obtain s-LA-ITO.

Synthesis of m-LA-IO. The synthesis of m-LA-IO followed the same process of s-LA-ITO mentioned above, except that the $SnCl_4$ was not added.

Synthesis of w-LA-ITO. w-LA-ITO refers to as-received commercial ITO, which was used without further modification.

***In situ* ATR-SEIRAS measurements.** *In situ* ATR-SEIRAS spectra were performed in a conventional H-cell on a FTIR spectrometer (Bruker 70 V). The working electrode was prepared by drop-casting catalyst ink onto Au coated Si hemispherical prism. An Ag/AgCl electrode was used as the reference electrode and a Pt wire was used as the counter electrode. *In situ* ATR-SEIRAS spectra were recorded with a resolution of 8 cm^{-1} from 0 to -0.9 V *vs.* RHE in the Series mode of OMNIC.

***Operando* Raman measurements.** *Operando* Raman spectra were acquired in a custom-designed spectroelectrochemical MEA cell following a previously reported configuration[40]. The cell was assembled using a 1-cm^2 IrO_2-coated Ti mesh as the anode, a PiperION A20 anion exchange membrane (1.5 cm × 2.0 cm), and a 1-cm^2 gas diffusion electrode as the cathode (Sigracet 29BC, 2 mg cm^{-2}), which presented a well-defined catalyst layer interface for cross-sectional observation. 20

mM Cs_2CO_3 solution served as the anodic electrolyte. The AEM was laid over the anode plate, then mechanically sealed against a gas-tight quartz observation window *via* fastening components (Supplementary Fig. 33).

For each independent test, the liquid flow rate of the anolyte was stabilized at 0.5 mL min^{-1}, and humidified CO_2 (20 mL min^{-1}, room-temperature bubbler) was delivered to the cathode. The confocal laser was precisely focused onto target regions within the catalyst layer (CL) during data acquisition. To establish stable electrochemical reduction conditions, the cell was pre-electrolyzed at 10 mA cm^{-2} for 5 min prior to the initial Raman scan. Raman measurements were then carried out sequentially at current densities of 20, 50, 100, 200 and 300 mA cm^{-2}, with an approximately 2-minute stabilization period at each step before spectral acquisition. A 1-min waiting period was imposed after each current jump to enable full system equilibration before recording corresponding Raman spectra. To eliminate spectral influence from irreversible catalyst structural reconstruction, all operando spectral datasets acquired at identical CL positions were replicated in separate parallel electrochemical trials.

All *operando* Raman spectra were recorded on a Horiba Jobin Yvon XploRA Plus confocal Raman spectrometer equipped with a 638 nm excitation laser, a ×50 objective lens (NA = 0.5) and a CCD detector. The laser power was attenuated to 10% of the nominal output to prevent laser-triggered interfacial structural damage to the electrode, and the integration time was fixed at 15 s per spectrum.

Electrochemical measurements of CO_2RR. All the electrochemical measurements of CO_2RR were performed by an electrochemical workstation (CHI 660E). In a three-electrode flow cell, CO_2RR performances were conducted in 0.5 M $KHCO_3$ electrolytes with Ag/AgCl as the reference electrode and IrO_x/Ti as the counter electrode. A gas-diffusion electrode (GDE, Sigracet 29BC) with the catalysts ink (1 mg cm^{-2}) brushed on was served as the working electrode, in which the catalysts ink contained catalysts and Nafion (Dupont, 5%). An anion-exchange membrane (Sustainion X37-50 RT) was located to separate the cathode and anode.

In a typical two-electrode MEA electrolyzer (5 cm^2, Dioxide Materials), a IrO_x/Ti foam served as the anode electrode and a GDE (Sigracet 29BC) with the catalysts ink (2 mg cm^{-2}) brushed on was served as the cathode electrode, in which the catalysts ink contained catalysts, VXC-72 Cabot black carbon (0.1 mg cm^{-2}) and Nafion (5%). An anion-exchange membrane (Sustainion X37-50 RT) was located to separate the cathode and anode. The anode electrolyte was single-pass 20 mM Cs_2CO_3.

Details related to electrochemical measurements were displayed in Supporting Information.

References

1. Fang, W. *et al*. Durable CO_2 conversion in the proton-exchange membrane system. *Nature*. **626**, 86-91 (2024).
2. Li, J. *et al*. Molecular-scale CO spillover on a dual-site electrocatalyst enhances methanol production from CO_2 reduction. *Nat. Nanotechnol.* **20**, 515-522 (2025).
3. Ram, R. *et al*. Water-hydroxide trapping in cobalt tungstate for proton exchange membrane water electrolysis. *Science*. **384**, 1373-1380 (2024).
4. Yang, X. *et al*. Atomically dispersed cerium on copper tailors interfacial water structure for efficient CO-to-acetate electroreduction. *Nat. Commun.* **16**, 2811 (2025).
5. Hao, S. *et al*. Acid-humidified CO_2 gas input for stable electrochemical CO_2 reduction reaction. *Science*. **388**, eadr3834 (2025).

6. Fan, L. *et al*. Atomic-level Cu active sites enable energy-efficient CO_2 electroreduction to multicarbon products in strong acid. *Nat. Synth*. **4**, 262-270 (2025).
7. Wen, Y. *et al*. Zeolite-confined Cu single-atom clusters stably catalyse CO to acetate at 1 A cm^{-2} beyond 1,000 h. *Nat. Nanotechnol.***20**, 656-663 (2025).
8. Cai, Y. *et al*. Self-pressurizing nanoscale capsule catalysts for CO_2 electroreduction to acetate or propanol. *Nat. Synth*. **3**, 891-902 (2024).
9. Guerra, O. J. *et al*. Barriers and opportunities for the deployment of CO_2 electrolysis in net-zero emissions energy systems. *Joule*. **7**, 1111-1133 (2023).
10. Li, Z. *et al*. Electroreduction-driven distorted nanotwins activate pure Cu for efficient hydrogen evolution. *Nat. Mater.* **24**, 424-432 (2025).
11. Niu, W. *et al*. Reaction-driven restructuring of defective $PtSe_2$ into ultrastable catalyst for the oxygen reduction reaction. *Nat. Mater.* **23**, 1704-1711 (2024).
12. Yu, S. *et al*. CO_2-to-methanol electroconversion on a molecular cobalt catalyst facilitated by acidic cations. *Nat. Catal.* **7**, 1000-1009 (2024).
13. Wei, P. *et al*. Coverage-driven selectivity switch from ethylene to acetate in high-rate CO_2/CO electrolysis. *Nat. Nanotechnol.* **18**, 299-306 (2023).
14. Albertini, P. P. *et al*. Hybrid oxide coatings generate stable Cu catalysts for CO_2 electroreduction. *Nat. Mater.* **23**, 680-687 (2024).
15. Tan, X. *et al*. Stabilizing Copper by a Reconstruction-Resistant Atomic Cu-O-Si Interface for Electrochemical CO_2 Reduction. *J. Am. Chem. Soc.* **145**, 8656-8664 (2023).
16. Kok, J. *et al*. Interrogation of Oxidative Pulsed Methods for the Stabilization of Copper Electrodes for CO_2 Electrolysis. *J. Am. Chem. Soc.* **146**, 19509-19520 (2024).
17. Li, L. *et al*. Stable, active CO_2 reduction to formate *via* redox-modulated stabilization of active sites. *Nat. Commun.* **12**, 5223 (2021).
18. Yan, S. *et al*. Electron Localization and Lattice Strain Induced by Surface Lithium Doping Enable Ampere-Level Electrosynthesis of Formate from CO_2. *Angew. Chem. Int. Ed*. **60**, 25741-25745 (2021).
19. Yuan, Y. *et al*. *In Situ* Structural Reconstruction to Generate the Active Sites for CO_2 Electroreduction on Bismuth Ultrathin Nanosheets. *Adv. Energy Mater.* **12**, 2200970 (2022).
20. Hu, L. *et al*. A scalable membrane electrode assembly architecture for efficient electrochemical conversion of CO_2 to formic acid. *Nat. Commun.* **14**, 7605 (2023).
21. Shen, H. *et al*. Theoretical calculation guided design of single atom-alloyed bismuth catalysts for ampere-level CO_2 electrolysis to formate. *App. Catal. B: Environ*. **339**, 123140 (2023).
22. Shen, H. *et al*. *In-Situ* Constructing of Copper-Doped Bismuth Catalyst for Highly Efficient CO_2 Electrolysis to Formate in Ampere-Level. *Adv. Energy Mater.* **13**, 2202818 (2023).
23. Bi, J. *et al*. High-Rate CO_2 Electrolysis to Formic Acid over a Wide Potential Window: An Electrocatalyst Comprised of Indium Nanoparticles on Chitosan-Derived Graphene. *Angew. Chem. Int. Ed*. **62**, e202307612 (2023).
24. Zhang, Q. *et al*. Atomic dynamics of electrified solid-liquid interfaces in liquid-cell TEM. *Nature*. **630**, 643-647 (2024).

25. Wang, D. *et al*. Revealing the structural evolution of CuAg composites during electrochemical carbon monoxide reduction. *Nat. Commun.* **15**, 4692 (2024).

26. Fu, Q. *et al*. Unraveling and leveraging *in situ* surface amorphization for enhanced hydrogen evolution reaction in alkaline media. *Nat. Commun.* **14**, 6462 (2023).

27. Shi, Y. *et al*. Combination of nanoparticles with single-metal sites synergistically boosts co-catalyzed formic acid dehydrogenation. *Nat. Commun*. **15**, 8189 (2024).

28. Zheng, H. *et al*. Understanding the Affinity Effect of C/O-Correlative Intermediates for the Selective Electrosynthesis of HCOOH. *ACS Catal*. **15**, 16156-16164 (2025).

29. Cheng, Y. *et al*. Integrated Capture and Electroreduction of Flue Gas CO_2 to Formate Using Amine Functionalized SnO_x Nanoparticles. *Acs Energy Lett.* **6**, 3352-3358 (2021).

30. Sun, B. *et al*. Unveiling pH-Dependent Adsorption Strength of $*CO_2^-$ Intermediate over High-Density Sn Single Atom Catalyst for Acidic CO_2-to-HCOOH Electroreduction. *Angew. Chem. Int. Ed*. **63**, e202318874 (2024).

31. Cheng, H. *et al*. Surface Nitrogen-Injection Engineering for High Formation Rate of CO_2 Reduction to Formate. *Nano Lett.* **20**, 6097-6103 (2020).

32. Zu, X. *et al*. Efficient and Robust Carbon Dioxide Electroreduction Enabled by Atomically Dispersed $Sn^{\delta+}$ Sites. *Adv. Mater.* **31**, 1808135 (2019).

33. Wang, Y. H. *et al*. *In situ* Raman spectroscopy reveals the structure and dissociation of interfacial water. *Nature*. **600**, 81-85 (2021).

34. Sun, Q. *et al*. Understanding hydrogen electrocatalysis by probing the hydrogen-bond network of water at the electrified Pt-solution interface. *Nat. Energy*. **8**, 859-869 (2023).

35. Chen, X. *et al*. Revealing the role of interfacial water and key intermediates at ruthenium surfaces in the alkaline hydrogen evolution reaction. *Nat. Commun.* **14**, 5289 (2023).

36. Ledezma-Yanez, I. *et al*. Interfacial water reorganization as a pH-dependent descriptor of the hydrogen evolution rate on platinum electrodes. *Nat. Energy*. **2**, 17031 (2017).

37. Li, P. *et al*. Hydrogen bond network connectivity in the electric double layer dominates the kinetic pH effect in hydrogen electrocatalysis on Pt. *Nat. Catal.* **5**, 900-911 (2022).

38. Zhang, H. *et al*. Promoting Cu-catalysed CO_2 electroreduction to multicarbon products by tuning the activity of H_2O. *Nat. Catal.* **6**, 807-817 (2023).

39. Sun, K. *et al*. Interfacial water engineering boosts neutral water reduction. *Nat. Commun*. **13**, 6260 (2022).

40. Fu, L. *et al*. Distribution of Speciation and Activity Across the Catalyst Layer during CO_2 Electroreduction in Membrane Electrode Assembly. *Acs Energy Lett*. **10**, 3445-3450 (2025).

Data availability

The data supporting the findings of this study are available within the article and its Supplementary Information files.

Acknowledgments

This work was financially supported by the National Science Fund for Distinguished Young Scholars, Fundamental and Interdisciplinary Disciplines Breakthrough Plan of the Ministry of

Education of China, Beijing Outstanding Young Scientist Program (JWZQ20240102004), the National Science Fund for Young Scholars (No. 22409009), the Beijing Natural Science Foundation (No. Z220020), Tencent Foundation through the XPLORER PRIZE, CNPC Innovation Found (2021DQ02-1002) and China Postdoctoral Science Foundation (Grant No. 2023M730052). The authors thank the photoemission photoendstations BL11B and BL14W1 in the Shanghai Synchrotron Radiation Facility (SSRF) for the help with XAFS characterizations.

Author contributions

S.G. conceived the project. N.Y. and M.L. designed the research, and performed the material synthesis, characterization ad electrochemical tests. K.W., Y.T., Z.Q., Z.L., F.L., C.W. and Q.H. participated in the assemble and tests of MEA. N.Y. and Y.L. carried out the XAFS data analysis. H.G., C.S., Y.H. and C.Z. performed the HAADF-STEM characterization. L.L. and Y.G. conducted the DFT calculations. S.G. and N.Y. wrote the paper. All authors participated in the project discussions and production of the final manuscript.

Competing interests

The authors declare no competing interests.

Supplementary Files

This is a list of supplementary files associated with this preprint. Click to download.

- TEA.pdf
- RevisedSupportinginformation.pdf